



Available online at www.sciencedirect.com



NIM:A

NUCLEAR INSTRUMENTS AND METHODS IN PHYSICS RESEARCH 00 (2018) 1–15

Characterization of Novel Rotating Scatter Mask Designs for Gamma Direction Identification

Robert J. Olesen^a, Buckley E. O'Day^a, Darren E. Holland^{a,b}, Larry W. Burggraaf^a, James E. Bevins^a

^arobert.olesen@afit.edu

Department of Engineering Physics
Air Force Institute of Technology
Wright-Patterson AFB, OH

^bDepartment of Mechanical Engineering
Cedarville University
Cedarville, OH

Abstract

The Rotating Scatter Mask system is a low cost, directional radiation detection system with a nearly 4π field-of-view over a broad range of photon energies. However, the original mask design is limited by numerous similarities in the detector response directional modes. These similarities introduce potential misidentification errors when determining a source's direction. Previous studies identified a better mask design, the Mace, which significantly reduced the similarities between the modes. In this work, a new design class was simulated and compared to the Mace mask design using the modal assurance criterion to assess the differentiability between directional modes. At the expense of a slightly smaller field-of-view, these novel mask designs were shown to successfully decouple the angular components of the source's direction, improving the average criterion value by up to 83%. The new designs also drastically improved the system's efficiency, reducing the time to identify the source's direction by up to 64%, while enabling a simplified, alternative algorithm for identifying the source direction. This alternative approach, called the geometric correlation method, further improved detection efficiency leading to a near-real time analysis for locating a source direction with the Rotating Scatter Mask.

Keywords: RSM, design characterization, gamma imaging, source direction

1. Introduction

Directionally-sensitive radiation detectors have been shown to greatly improve the search efficiency over standard, “dumb” detectors [1], leading to the development of various gamma ray imaging systems. However, most of these systems are expensive, complex, and limited by the resolution or field-of-view (FOV). Collimators and coded aperture approaches use attenuating material to create patterns on a detector system, which are then used to image the source. By attenuating the signal, these systems inherently have low efficiencies and a small FOV [2, 3]. These systems can also be large, as demonstrated by the 3,500 lb 57-NaI detector Large-Area Coded-Aperture Gamma-Ray Imager [4] or the SuperMISTI [5] with a 32,000 lb 78-NaI detector imaging subsystem. Compton cameras (or Compton imagers) have become a popular gamma-ray imaging system due to a 4π steradian FOV [6] and capability to isolate background signatures [2, 7]. However, as these devices rely on Compton scattering events, they are subject to low efficiencies and photon energy sensitivity.

The Rotating Scatter Mask (RSM) was developed as an inexpensive, simple detection system capable of determining a gamma-emitting source's direction using a single standard NaI detector with a near 4π field-of-view

(FOV) [8, 9]. The RSM system utilizes a geometrically varying polymethacrylate mask placed over a single position-insensitive NaI detector, as shown in Fig. 1. The mask is rotated about the detector at a set, constant rate thereby generating unique source position dependent spectra, referred to as detector response curves (DRCs). Similar to coded aperture approaches, the DRCs can be used to determine the source's direction through a maximum likelihood approach.

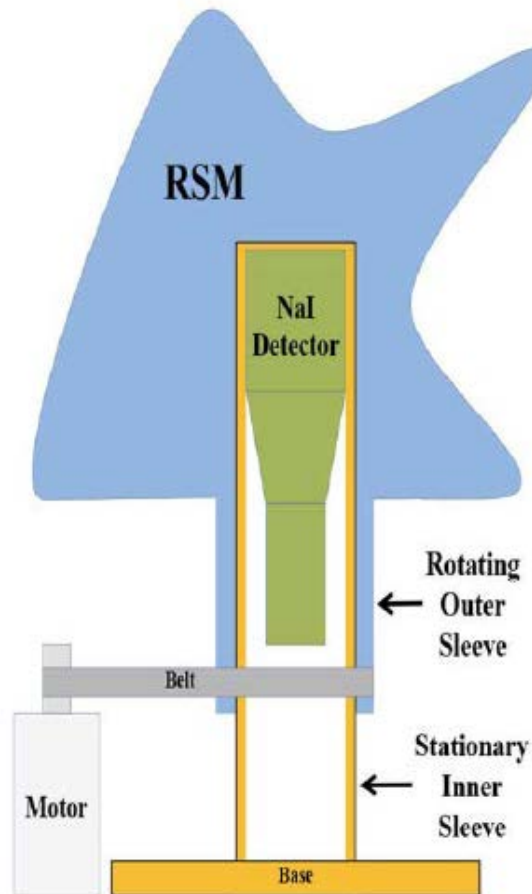


Fig. 1. The main components of the RSM system: the rotating polymethacrylate mask (with rotating sleeve of the same material), stationary NaI detector, aluminum sheath housing the detector, and the motor-belt system used to rotate the mask (color online).

FitzGerald [8] introduced and designed the first RSM concept, while Logan et al. [9] conducted the first experiments using the design and demonstrated statistical agreement between GEANT4 [10] simulations and experiments. Although Fitzgerald and Logan verified the original RSM design as a proof-of-concept, the RSM performance was limited by similarities in the DRC modes, resulting in degenerate solutions indicating several possible source directions. Holland et al. [11] further improved the system by optimizing the RSM geometry through a comprehensive design analysis which minimized these modal similarities. Further improvements were suggested but not tested. This works further advances the RSM design characterization through exploration of different designs and development of new analysis techniques that improve the RSM system by limiting degenerate solutions and maximizing detection and computational efficiency.

The remainder of the paper is organized in the following sections. A brief overview of the design process and methodologies used to generate and test a new class of RSM designs is given in Section 2. Section 3 compares

30 the new designs' performance with previous designs and investigates an alternative identification algorithm based on the specific proposed class of RSM geometries. Finally, Section 4 summarizes the key findings from the study and discusses future areas of research for the RSM system.

2. RSM Design

35 The new RSM geometries were created by modifying the discrete voxel method developed by Holland et al. [11]. In this method, a three-dimensional mesh of the geometry was mapped onto a two-dimensional matrix, where each element of the matrix corresponded to a hexahedral voxel. In this manner, any sized $m \times n$ matrix could be converted into a 3D model. A spherical coordinate system was used to describe the system where θ represented the azimuthal angle, the rotational component of the RSM, and ϕ represented the polar angle. The DRCs were designed such that the curve's shape varied based on the source's ϕ direction; a change in θ for sources at a fixed ϕ corresponded to a simple 40 shift in the DRC. Thus, the general shape of a given Φ DRC mode are invariant of the θ direction. It is important to distinguish this work's nomenclature: the symbol ϕ refers to the source's actual polar direction, while Φ refers to the invariant, modal DRC of the RSM system generated by the source at an angle of ϕ for any θ position.

An aluminum sheath with an approximately 3.81 cm inner radius and 4 cm outer radius housed the detector, photomultiplier tube (PMT), and electrical connections. A hollow cylindrical sleeve of the same polymethacrylate material provided structural support and a connection to the motor-belt system, as shown in Fig. 1. With an inner radius of 4 cm and a thickness of 1 cm, the support sleeve created a consistent contact between the mask and stationary aluminum sheath housing the detector without significantly reducing the number of counts detected. This sleeve and the RSM can be manufactured as a single homogeneous unit that can easily be attached to and detached from the detector system.

50 To account for the motor assembly and electronics behind the RSM, a maximum polar angle of 170° was chosen for each mask. This created a small region in which the RSM could not image, thereby reducing the FOV. In practical applications, the RSM can easily be oriented such that this region has no significant impact on source identification (i.e. the RSM can be oriented vertically so that the blindspot is directed towards the ground and only images a small area). Since the blindspot only spanned a solid angle of $\approx 0.1\pi$ steradians, the FOV was still 99% of a full 4π , 55 effectively equal to the performance of Compton cameras [6]. It should be noted that this blindspot is characteristic of the mask design; any electrical and mechanical components may introduce further limitations to the FOV. As the focus of this study was to characterize just the mask design, these components and their effects were neglected in this study.

2.1. Modal Assurance Criterion

60 The Modal Assurance Criterion (MAC) was used as the RSM mask design's evaluation criterion to evaluate similarities between DRCs. Ranging from zero to one, the MAC describes the similarity between two modal vectors [12]. A value of one indicates that two modes are completely consistent, while a value of zero indicates orthogonality. As the MAC is a normalized unit, the value between any two modes is independent of the modes' magnitudes. It is, therefore, a useful figure of merit for this system where the strength of the signal will vary based on the source 65 strength, distance, and average attenuation throughout the different Φ DRC modes. For this study, the MAC value was defined as

$$MAC_{i,j} = \frac{(\mathbf{u}_i^T \mathbf{u}_j)^2}{(\mathbf{u}_i^T \mathbf{u}_i)(\mathbf{u}_j^T \mathbf{u}_j)}, \quad (1)$$

where \mathbf{u}_i was the discretized reduced DRCs for the given Φ_i DRC. The reduced DRCs were calculated by subtracting the mean number of counts in each Φ DRC. This served to help reduce the bias in the MAC value comparisons caused by the minimum number of counts detected throughout the mask rotation [11].

70 As there is no *a priori* knowledge of the starting θ position of the source, the MAC value must be calculated for every θ shifted combination of two DRCs. The maximum MAC, M_{max} , resulting from these comparisons indicates the maximum overlap of two DRCs. Similar to maximum likelihood estimators, M_{max} can be used to determine the source's direction by collecting a sample DRC and calculating the M_{max} value between it and every Φ DRC mode in a

database, under all possible θ shifts. The combination that produces the overall maximum M_{max} signifies the source's
 75 ϕ direction while the θ shift required to best match the sample and database DRCs signifies the source's θ direction.
 Using this method, an optimal RSM design would have $MAC_{i,j} = 0$ for $i \neq j$ and $MAC_{i,j} = 1$ only when $i = j$.

2.2. Previous Design Methodologies

To create the RSM geometries, Holland et al. [11] developed two general design classes, referred here as the Eigen and Spartan classes. In the Eigen class, both θ and ϕ are simultaneously identified from a single M_{max} , as previously
 80 described. Two approaches were taken to minimize DRC similarities caused by the required θ shift comparisons for Eigen class designs: an eigenvector approach, which created a design matrix derived from a mass-spring eigenvalue problem, and a binary approach, which created a design matrix of ones and zeros. Both approaches were shown to successfully reduce the DRC Φ mode similarities, but the eigenvector approached was shown to be the most successful. It had a significant 68% reduction in the average M_{max} at the expense of a 21% decrease in detection efficiency. This
 85 improved design was named the Mace RSM and was chosen as the baseline comparison for new designs in this study.

The Spartan class introduced a “geometrical marker” [11] in the form of a physical wall in the RSM geometry. This wall created a consistent, low measurement response when it was inline between the source and detector. The source's θ direction was identified based on where this minimum response occurred in the DRC along the RSM rotation. Once θ was known, the measured and database DRCs could be calibrated to a comparison reference θ
 90 position (i.e. shifting the DRC minimum to $\theta = 0^\circ$). This step eliminated the need to calculate M_{max} for every shifted combination, reducing the number of comparisons from $m \times n$ to simply n , and potentially minimizing M_{max} between different DRCs. Effectively, this class decoupled θ and ϕ , and a linearly independent basis set could theoretically be created such that the DRCs are completely orthogonal.

A Hadamard matrix [13] was originally used as the basis set for this class [11]. For this design, the M_{max} actually
 95 increased from the original Fitzgerald RSM, even when θ was decoupled. However, this class was not as rigorously optimized as the Eigen class designs and was left for further research.

2.3. New Spartan Class Design Methodologies

This study seeks to further the characterization of the Spartan class RSMs through simulation of the RSM geometries described in the following sections. Section 2.3.1 describes three new Spartan class designs developed through
 100 the combination of aspects of the eigenvalue and binary approach with the Spartan class RSMs. Section 2.3.2 describes four new Spartan class designs developed though use of the geometrical marker approach to both decouple θ and determine ϕ without requiring any M_{max} calculations. For the designs shown in Section 2.3.1 and 2.3.2, the wall was designed with a thickness of 20 cm to maintain the scale of previous studies [11] and the original FitzGerald RSM [8, 9].

105 2.3.1. Eigen- and Binary-Based Approach

The goal of the RSMs in this section was to combine the advantages of the Eigen class's orthogonal basis sets and the decoupling capability of the geometric marker. The three RSM designs chosen, the Mace II, Modal Binary, and Spaced Binary, are presented in Fig. 2. The figure shows the prominent feature of the Spartan Class, the wall, on the ride side of each RSM. In the simulations, $\theta = 0^\circ$ was chosen to be along the closest wall edge.

110 As their names suggest, these three geometries were based on the Mace (eigenvalue approach) and binary RSM designs described in 2.2. Mace II used the same design matrix as the Mace at a one-half scale (10 cm maximum) in order to include the 20 cm wall. The half scale was also chosen to improve the design's efficiency, which was one of the limiting factors from the original Mace RSM. The motivation behind the Mace II was similar to the Hadamard approach: by leveraging the decoupling from the wall, the basis set of the original Mace design could be utilized to its maximum without the dependency issues caused by θ shifting. Each voxel of the Mace II mask spanned 12° in θ and 5.15° in ϕ , corresponding to a 33×30 design matrix.

115 The two binary geometries used basis sets comprised of ones and zeros. The Spaced Binary design was created using the simplest orthogonal basis set with just one non-zero element along each θ rotation. However, unlike the Binary design discussed in the next section, the Spaced Binary included gaps between the non-zero elements. This gap was thought to improve the orthogonality of the DRCs by increasing the separation of the Φ DRCs and reducing the amount of overlap in the DRC shapes. The Modal Binary design used an increasing number of non-zero elements, all

with equal heights (10 cm). This was done to mimic the orthogonality of sinusoidal waves with different frequencies, under the assumption that the DRCs from this geometry would follow similar shapes based on the periodic nature of the design. Gaps were also included for the same reasoning as the Spaced Binary. Both the Spaced Binary and Modal Binary used a 36×17 design matrix, corresponding to a 10° discretization in both θ and ϕ .
 125

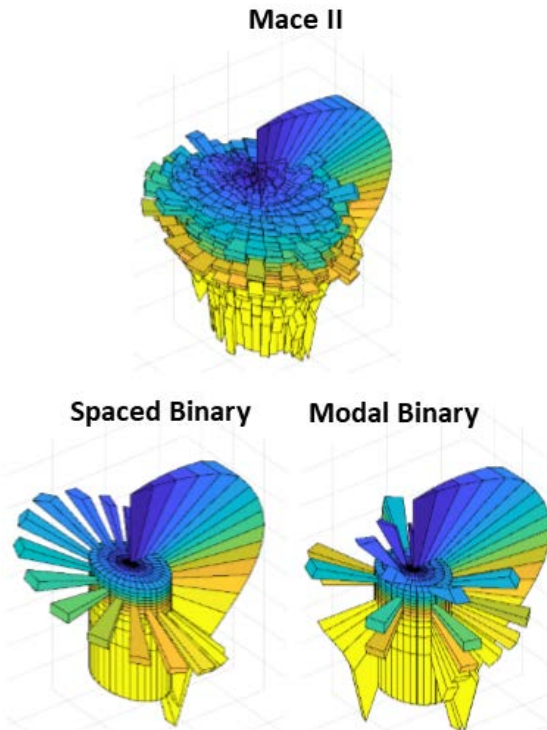


Fig. 2. The three Spartan class designs based on the eigenvalue Mace solution (top) and binary approaches (bottom). The wall common to each design is used to decouple θ (color online).

2.3.2. Geometric Correlation Approach

The next four geometries were created with the intent of using the geometrical marker concept to identify both θ and ϕ . Unlike the designs in the previous section, these RSMs were designed to determine the source direction without requiring any MAC value calculations (thereby eliminating the need for orthogonal DRCs). Fig. 3 shows the four similar Binary, Tall Wall, Wide Wall, and Large Fin RSMs. These are also closely related to the binary approach; however, these were designed specifically such that a second wall spiraled down the side of the mask. This spiral, designated as the “fin”, was intended to act as a secondary geometrical marker for the ϕ direction. The fin was created for two reasons. First, the design matrix for the fin would decrease M_{max} as it represents a semi-orthogonal basis set, similar to the Spaced and Modal Binary designs. Second, a different method could be used to identify the ϕ similar to how θ was calculated from the location of the wall valley. This can be achieved due to the linearly increasing distance between the wall and fin as ϕ increases, creating a second low measurement response along the DRC. The specific algorithm used for these designs is discussed in detail in Section 3.2. The thickness of the fin and angular width of the wall and fin were varied in these four designs to characterize their effects on the angular decoupling, system efficiency, and capability to identify θ and ϕ separately.
 130
 135

2.4. Design Evaluation

Theoretical response curves were generated for the seven new RSM designs through MCNP6.1.4 simulations [14]. The MCNP models were validated through comparison to another transport code, GEANT4 [10], as well as experimental data from the FitzGerald device [9]. For consistency with previous studies [9, 11], the simulation used

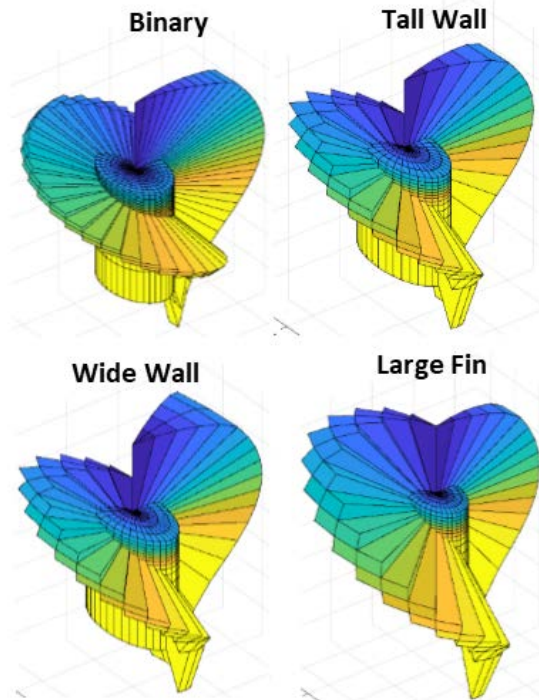


Fig. 3. The four Spartan class designs used to decouple both θ and ϕ using a linear correlation between the distance between the fin and wall as ϕ increases. The multiple designs were chosen to study the effect of wall and fin size on the RSM efficiency and ability to decouple the angular components (color online).

a monoenergetic point source of 662 keV at a distance of 86.36 cm from the detector to model a ^{137}Cs source. The simplified RSM assembly modeled in MCNP only included the polymethacrylate mask and support shell, 3 x 3" NaI crystal, and aluminum sheath.

The DRCs were calculated by varying the source location in 5° increments in θ and ϕ and using a MCNP pulse height tally in the NaI crystal with 1 keV energy bins. The DRCs were then generated by collecting the number of tallies (photon counts) in the 662 keV energy bin, corresponding to the full-energy peak (FEP) of the ^{137}Cs , at each source direction. A total of 500,000 particle histories were conducted for each run in order to reduce the relative uncertainty in the number of counts in the FEP to a maximum of 4.5% for all designs over all source directions.

In order to improve the computational efficiency, the source particles were limited to a cone centered on the detector. This variance reduction technique neglects any scatters in the air or mask that may then interact in the crystal. However, only photons that proceed unimpeded from the source to the crystal can contribute to the FEP, as any scatter removes energy from the photons and results in a tally in a lower energy bin. This was also why the mechanical components of the RSM were not modeled, as any scattered photons from those components would not have contributed to the FEP.

Two figures of merit were generated in order to characterize the performance of the seven RSMs. The average M_{max} between all different Φ DRC pair comparisons designated \bar{M}_{max} , is an approximate estimate of the overall performance of the RSM. This value excludes the $M_{max} = 1$ terms resulting from comparing the same Φ DRC to itself; the ideal value \bar{M}_{max} is zero. The average number of counts detected within the FEP per photon emitted by an isotropic sources over all source directions, C , measures the average efficiency of the system. A higher C value indicates better detection efficiency. Therefore, optimizing the RSM design involves minimizing \bar{M}_{max} while maximizing C . These two values were used to compare against the baseline Mace design.

165 **3. Results and Analysis**

Fig. 4 shows the four M_{max} plots resulting from simulations using the FitzGerald, Mace, Modal Binary, and Wide Wall RSM designs. These plots were generated with no assumption on angular decoupling and show the calculated MAC value for every θ shift possibility as described in Section 2.1. This allows a direct comparison to the Mace RSMs. Note that the diagonal terms are always equal to one, regardless of the design, as those values corresponded to comparing a Φ modes to itself, which is why they were excluded in calculating \bar{M}_{max} . Second, the plots are also symmetric about the diagonal, as shown in Eq. 1. Thus, the symmetric values are omitted for clarity in the M_{max} plots.

170

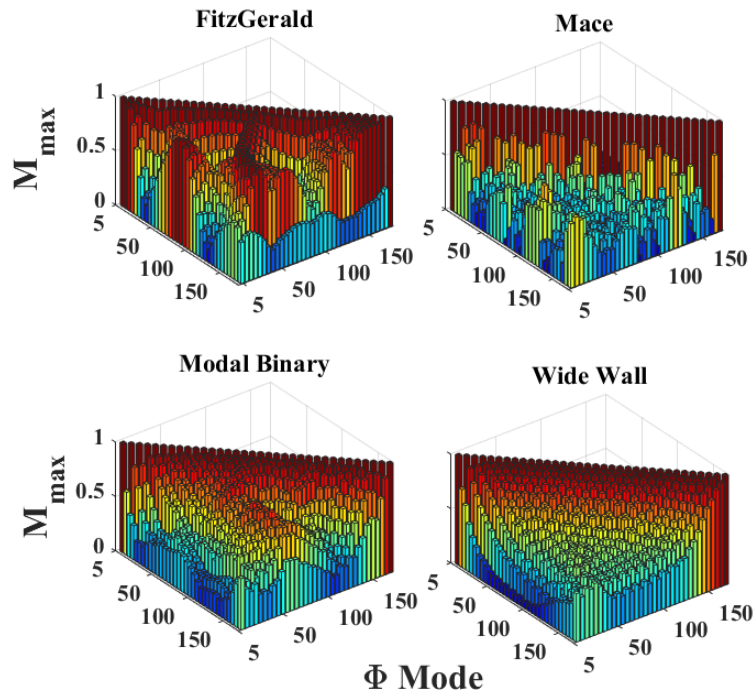


Fig. 4. Four example M_{max} plots showing the degree of similarity between the Φ modes. The FitzGerald (top left) has many regions where $M_{max} \approx 1$, causing potential mis-identification in the source directions. The other designs reduce the magnitude and number of regions where this occurs (color online).

The plots serve as an easy visual indication of the performance of the RSM when simultaneously identifying θ and ϕ . The FitzGerald plot demonstrates its limitations, as several degenerate regions are clearly visible. In practice, this indicates multiple possible source directions would be identified. The Mace RSM significantly reduced M_{max} between the DRCs.

175

Table 1 summarizes the results for the Mace and the seven new Spartan class designs. Without decoupling, the new designs had larger values of \bar{M}_{max} than the Mace, ranging from a 36 – 90% increase, but improved the overall system efficiency by 26 – 66% due to the smaller volume of the Spartan class masks. The relatively high \bar{M}_{max} was expected as the Spartan Class RSMs were not designed to optimize M_{max} , which was a primary design driver for the Mace RSM. However, the Spartan class designs’ \bar{M}_{max} can be improved by taking advantage of their unique DRC features.

180

3.1. Spartan Analysis

Fig. 5 shows an example Modal Binary RSM DRC for the $\Phi = 110^\circ$ mode used in the calculation of the decoupled M_{max} shown in Fig. 6. There is a notable “valley” of counts centered around $\theta = 5^\circ$, corresponding to the center of the wall used in the design. All Spartan Class RSMs featured a similar valley located at the center of the wall. If the measured DRC matched Fig. 5, the θ position of the source would be identified as 5° . For any other θ position, the valley would be centered at that new θ angle, corresponding to the aforementioned shifting of the DRCs. However,

Table 1: Comparing average response of RSM designs using \bar{M}_{max} over all possible DRC combinations and the normalized count rate from an isotropic source, C .

Design	\bar{M}_{max}	$C(\times 10^{-4})$
Mace	0.314	1.36
Mace II	0.526	1.71
Modal Binary	0.598	2.20
Spaced Binary	0.580	2.18
Binary	0.428	2.26
Tall Wall	0.486	2.17
Wide Wall	0.577	2.13
Large Fin	0.510	2.13

unlike the Eigen class RSMs, this shift is easily detectable due to the valley, and, once identified, the DRC can then be re-shifted to the known reference case to calculate M_{max} (and ϕ) with no other shifts.

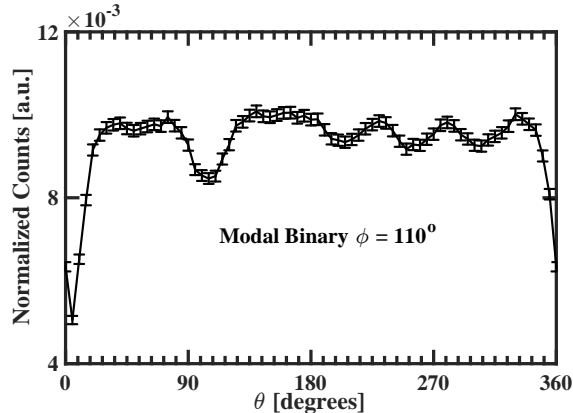


Fig. 5. Example DRC of a Spartan class design using the Modal Binary RSM at the $\Phi = 110^\circ$ mode. The wall valley can be clearly seen at $\theta = 5^\circ$.

190 The impact of this simplification is shown in the drastic M_{max} reduction in Fig. 6, using the results of the Large
Fin RSM. On the left are the M_{max} values over all possible θ shifts, the same plot used to calculate the average \bar{M}_{max}
in Table 1. On the right are the M_{max} values when no shifts are calculated, under the assumption that θ has been
decoupled and previously identified by the geometric marker. That is, only the MAC value of the DRCs for $\theta = 0^\circ$,
the reference position, were calculated. Using this technique, \bar{M}_{max} was reduced from 0.510 to 0.177 for the Large
195 Fin, a 44% increase in performance over the Mace RSM. This design shows almost ideal M_{max} behavior. As shown in
Figure 6, the off diagonal terms rapidly decrease to zero. At this level, the spread in the M_{max} surrounding the diagonal
approaches the RSM's physical resolution, 5° , and there are no other local maxima that would indicate degenerate
solutions and potential mis-identification issues. In other words, this RSM would be expected to always locate the
direction of the true source within an angular resolution of 5° in θ and ϕ .

200 In order to decouple θ , the wall valley must be distinguishable from the baseline and fin response in order to
precisely identify the location of θ , the valley minimum. Fig. 7 plots the DRCs for the Tall Wall design up to the
 $\Phi = 50^\circ$ mode. At low ϕ angles, the valley is indistinguishable from the rest of the DRC and the location of θ cannot
be determined. Only for Φ modes at and above 30° is the wall valley discernible with a definite minimum. This
205 result was consistent for every Spartan Class RSM, and is due to the cylindrical geometry of the NaI detector. It is
very likely this geometrical limitation poses similar issues in Eigen Class designs; however, the effects are much more
apparent in the Spartan Class RSMs due to the requirement for well defined minima to decouple θ and ϕ . As a result,
this method of decoupling θ only works for source positions with $30^\circ \leq \phi \leq 170^\circ$, limiting the FOV for the Spartan

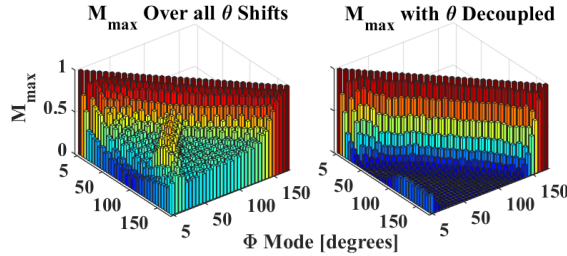


Fig. 6. Comparing M_{max} under all shifts (left) and when θ has been decoupled (right). By decoupling, M_{max} has been significantly reduced and the plot approaches an ideal response (color online).

Class to approximately 92.5% of a full 4π steradians. This is only a minor impact on performance as it still maintains a 360° view in θ .

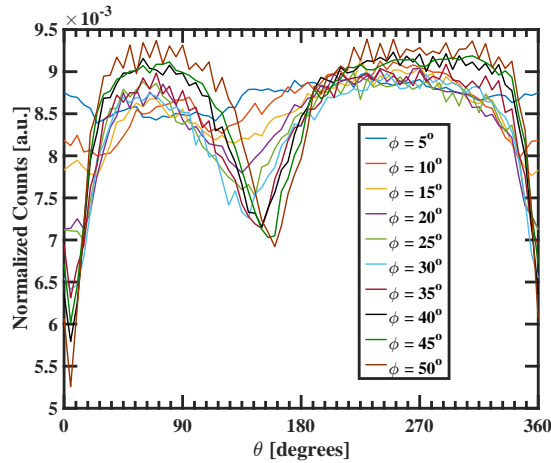


Fig. 7. The effect of the wall valley at low Φ modes for the Tall Wall design. Under 30° , the wall valley become indistinguishable and decoupling of θ cannot be done (color online).

210 3.1.1. Bias Reduction

Although Fig. 6 demonstrates that decoupling greatly improved the average M_{max} for the Large Fin RSM, most other Spartan Class RSMs showed only minor improvement in M_{max} as shown in Fig. 9. Fig. 9 shows a similar trend as the Large Fin plot, except that the off diagonal terms stagnate around 0.3. This was caused by the valley creating an unintended consistency in the Φ modes (a low value at $\theta = 5^\circ$ regardless of the specific DRC) as shown in 8. These valleys were required in order to decouple θ , but because they are in the same location for every DRC, there was an inherent similarity, or bias, in their shapes.

Since the detector response generated from the wall and from the rest of the mask are independent, the total DRC can be modeled as a linear combination of both responses. As a result, the wall valley region can be excluded from the MAC value calculations to help reduce the bias and emphasize the critical regions of the DRCs that are unique to each Φ DRC. Excluding the bias region for the Wide Wall RSM results in Fig. 10, with a large reduction in the M_{max} between the DRCs. This bias reduction method was repeated for all Spartan Class RSMs using the available Φ modes greater than 30° . The results of this bias reduction are summarized in Table 2.

The table shows that the Spartan class designs outperformed the Mace RSM under decoupling and bias reduction. Most notable is a significant decrease in \bar{M}_{max} for all Spartan class designs, improving 24%–66% over the Mace. The Mace II design reduced \bar{M}_{max} the most. As expected, the eigenvector-based design matrix combined with θ decoupling

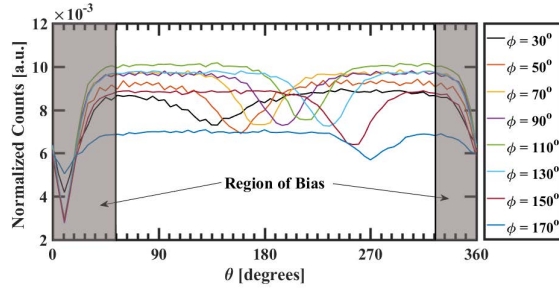


Fig. 8. Plot showing the region of bias introduced by the wall valley in the DRCs of the Wide Wall RSM. The shaded regions created a bias in the M_{max} due to their consistent shape in the DRC for every Φ mode. This is inherent to all Spartan class RSMs (color online).

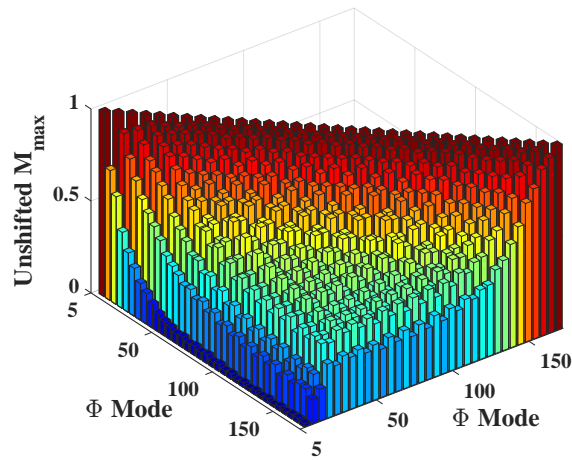


Fig. 9. M_{max} plot from the DRCs of the Wide Wall RSM. The bias region shown in Fig. 8 caused the MAC values to stagnate above a value of zero (color online).

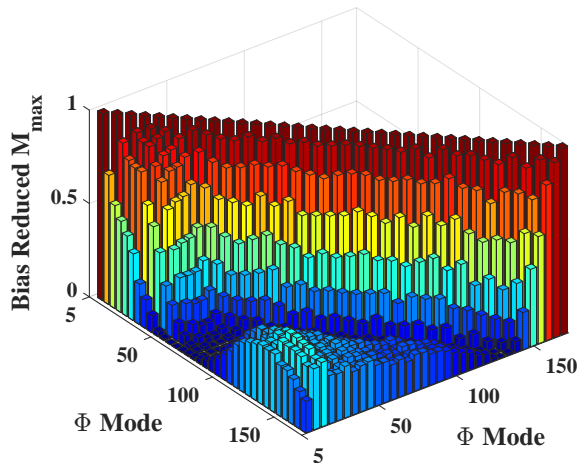


Fig. 10. Wide Wall RSM M_{max} computed after removing the bias region caused by the wall valley. By focusing on the regions unique to the Φ modes, the overall M_{max} was reduced. This procedure was repeated for all Spartan class RSMs (color online).

significantly decreased the similarity of the DRCs. Reducing the FOV to DRCs above $\Phi \geq 30^\circ$ had a minor effect on the average counts detected.

Table 2: Comparing average response of RSM designs after bias reduction using the Spartan Analysis technique.

Design	\bar{M}_{\max}	$C(\times 10^{-4})$
Mace	0.314	1.36
Mace II	0.106	1.69
Modal Binary	0.166	2.19
Spaced Binary	0.180	2.20
Binary	0.218	2.25
Tall Wall	0.234	2.18
Wide Wall	0.239	2.14
Large Fin	0.177	2.13

3.2. Alternative Detection Algorithm

The following section discusses a novel approach to identifying the source direction using the RSMs described in Fig. 3. With two geometrical markers, the DRCs of these designs contained two identifiable valleys. As shown in Fig. 11, the first valley corresponded to the low measurement zone caused by the vertical wall. The spiral fin created a similar, wider valley further along the DRC. As the distance between the wall and fin linearly increased with ϕ in these geometries, the distance between the two valleys should have followed a similar linear correlation. These distances were calculated for Φ DRCs $\geq 30^\circ$ for the Binary, Tall Wall, Wide Wall, and Large Fin designs. The distances were then fitted using a least-squares linear regression, and the distances and the fit are plotted in Fig. 12.

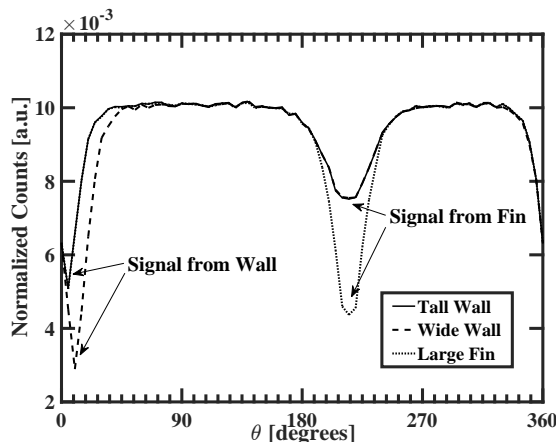


Fig. 11. Typical DRC of three Spartan class designs using the linear correlation between the wall and fin valleys. The two valleys act as independent geometrical markers for both θ and ϕ .

In all four designs, the distances between the two valleys showed a strong linear correlation to the Φ DRC. The adjusted R^2 for all the fits was above 0.99, showing good statistical agreement between the fit and data. Using these results, the following alternative algorithm is proposed in order to determine the source direction:

1. A FEP DRC is collected for a given point source of unknown direction.
 2. The θ direction is calculated by the location of the wall valley minimum along the rotation of the RSM. For all except the Large Fin design, this corresponds to the absolute minimum along the DRC. For the Large Fin, this is located in the shallower of the two valleys (Fig. 11).
 3. The ϕ direction is calculated by determining the distance between the two valleys and fitting them into the linear regression models of Fig. 12.
- With this method, θ and ϕ are calculated independently with no comparisons between the DRCs of other Φ DRC modes. This effectively eliminates any bias introduced in the modal shapes as well as the restrictions imposed on

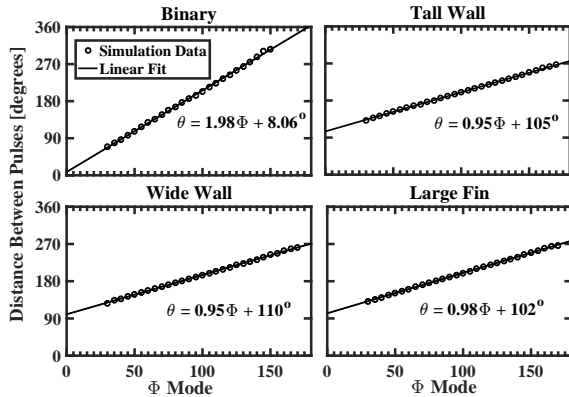


Fig. 12. Fitting the distance between the wall and fin valleys as a function of Φ . The strong linear correlation matches the geometric expectations of the four designs. This presents an alternative method for determining source direction over modal shape comparisons.

creating uniquely independent DRCs described in Section 2.1. The uncertainty in the source's direction is primarily limited to the spatial resolution of the DRC.

3.2.1. Detection Efficiency

As stated in Section 3.1.1, the Spartan Class RSMs improved the efficiency of the system due to the smaller mask size (less attenuation through the mask). This directly corresponds to a decrease in equivalent detection time required to achieve the same statistical certainty in the DRC as compared to the Mace RSM, by as much as 65% using the values in Table 2. This assumes that the entire DRC must be recorded within a certain statistical certainty in order to accurately compare the sampled DRC to the database.

However, the alternative algorithm described in Section 2.3.2 required only two points along the DRC, the minima in the wall and fin valley, to determine the source's direction. The requirement, therefore, is that a minimum number of counts must be collected such that the two valleys can be distinguished from each other in order to determine which angular component they correspond to. The uncertainty in counting is governed by Poisson statistics, so that the standard deviation in the number of counts is the square root of the number of counts detected. The requirement, then, to distinguish the two valleys must be that

$$N_2 - N_1 \geq s(\sqrt{N_1} + \sqrt{N_2}), \quad (2)$$

where N_1 is the absolute minimum in either the wall or fin valley, N_2 is the minimum of the shallower valley, and s is the number of standard deviations corresponding to the confidence level desired. This inequality is graphically represented in Fig. 13. The minimum number of counts required is then given by Equation 3, which solves for N_1 :

$$N_1 \geq \left(\frac{s}{\sqrt{r} - 1} \right)^2, \quad (3)$$

where the ratio of the valley counts, $r = N_2/N_1$ has been substituted in Equation 2.

The average valley ratios were calculated for the four RSM designs (with $\Phi \geq 30^\circ$), and \bar{N}_1 , the average DRC minimum, was computed at $s = 1, 2$, and 3σ confidence levels. The results are shown in Table 3. The Wide Wall RSM, due to its high average valley ratio, required the least number of counts in the wall valley minimum. At these low counts, the limiting factor becomes uncertainty in determining the actual valley minimum rather than distinguishing between the two valleys (equivalent to spatial resolution uncertainty). This spatial resolution problem is necessary in order to determine the accuracy and precision of this new source direction identification algorithm and is left for future work.

The time required, t , to measure a source that produces an absolute minimum N_1 in the DRC can be approximated with (in seconds):

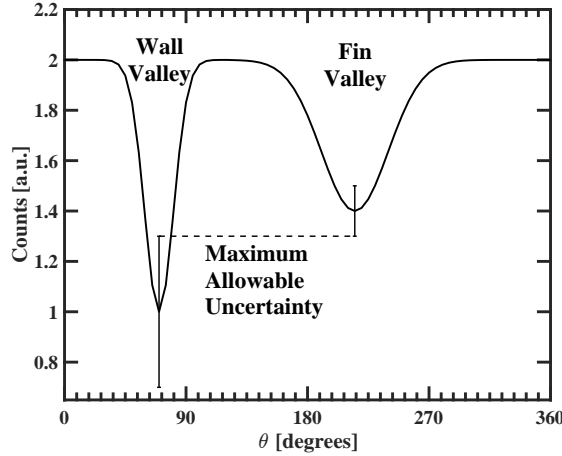


Fig. 13. Graphic representing the minimum number of counts necessary in order to distinguish between the wall and fin valley. This number of counts must be obtained in order to conduct the Spartan analysis or geometrical correlation methods.

Table 3: Comparing the absolute DRC minimum bin count required to distinguish the wall and fin valley.

Design	\bar{r}	$s = 1$	$s = 2$	$s = 3$
Binary	1.32	45	180	406
Tall Wall	1.27	62	248	559
Wide Wall	2.05	5	21	48
Large Fin	1.30	51	204	458

$$t \approx \left(\frac{R}{0.8636} \right)^2 \left(\frac{36N_1}{A C_{min}} \right), \quad (4)$$

where C_{min} is the number of counts detected at the minimum per particle emitted by an isotropic source, R is the distance from the center of the detector to the source, in m, and A is the activity of the source in Bq. The factor of 36 in the numerator of the second term accounts for the number of θ bins used to generate the DRC. For this equation, it was assumed that a minimum 36 bins of 10° increments in θ , corresponding to the spatial resolution of the voxels in the RSM design, are required in order to accurately generate the DRC. More bins corresponds to better resolution of the DRC, but as only two points are required, they are not necessary and just increase the collection time. The first term corrects for divergence of the source as distance increases from the detector, scaling to the 86.36 cm used in this study.

Using Equation 4, the average N_1 given in Table 3, and a $6 \mu\text{Ci}$ source 1 meter from the detector, the average detection times for the Binary, Tall Wall, Wide Wall, and Large Fin RSMs were calculated. The results, along with the average C_{min} values, are shown in Table 4.

Table 4: Comparing average collection time required to distinguish wall and fin valleys for a $6 \mu\text{Ci}$ source located one meter from the detector.

Design	$\bar{C}_{min} (\times 10^{-4})$	$s = 1$	$s = 2$	$s = 3$
Binary	1.52	64 s	257 s	581 s
Tall Wall	1.38	98 s	391 s	881 s
Wide Wall	0.87	13 s	53 s	120 s
Large Fin	1.07	104 s	415 s	931 s

285 The Wide Wall RSM showed the best performance in detection time, requiring just under a minute to achieve a 95% confidence level in distinguishing the two valleys. This is an 5 - 8 times better than any of the three other designs and a drastic improvement in efficiency over the previous detection algorithm using M_{max} calculations, which could take upwards of hours for a μCi source at the same distance. These results shows that these RSMs, in conjunction with the new source direction identification algorithm, could potentially be used for near-real time analysis, which no other RSM designs have achieved.

290 It should be noted that this time neglects any inefficiencies in the collection of counts from the NaI detector and pulse processing. These inefficiencies will invariably increase the detection time required and are dependent on the specific detection system used. Experiments are ongoing to characterize these effects.

4. Conclusions

295 Rotating Scatter Masks have demonstrated their usefulness as a low-cost, directional radiation detection system with a large field-of-view over a broad range of gamma energies. The original design was shown to exhibit degenerate solutions due to high degree of similarities in the directional modes of the detector response. Previous work was effective at reducing these similarities through the use of complicated, difficult to manufacture masks with relatively low detection efficiencies. However, the new proposed Spartan class improved the performance, efficiency, and 300 manufacturability over previous work.

In addition, by decoupling the angular components of the source direction, the analysis took advantage of the independence of the directional modes. Decoupling reduced the field-of-view for the Spartan class designs tested, which is most likely due to the cylindrical geometry of the NaI crystal. Practically, this created only a minor impact on the performance as the Spartan class designs still cover 92.5% of 4π and can be oriented such the the dead zone minimally impacts operations (i.e. vertically). The Spartan class also improved the system's efficiency, thereby 305 reducing the detection time required to determine the source's direction.

Finally, a subset of the Spartan class was able to determine both angular components of the source's direction without modal comparisons. This was achieved by creating a linear ϕ dependence in the distance between two valleys in the detector response, unique to the specific type of mask geometries from previous studies. The efficiency was 310 further improved under this method, leading to the potential for near-real time analysis using these designs.

The limiting resolution of the Spartan class has yet to be tested, and there will be uncertainty in determining the minima along the response curve. This uncertainty should be characterized by the width of the valleys. The Spartan class RSM size can also be reduced, potentially improving the efficiency further. Research and experiments are ongoing which will address these issues and help characterize the performance of the Rotating Scatter Mask in 315 practical applications.

Acknowledgments

This work was supported through the Defense Threat Reduction Agency, grant HDTRA-17-24526, and the U.S. Air Force Institute of Technology.

This research was supported in part by an appointment to the Faculty Research Participation Program at the U.S. 320 Air Force Institute of Technology, administered by the Oak Ridge Institute for Science and Education under contract DE-SC0014664 through an interagency agreement between the U.S. Department of Energy and AFIT.

- [1] R. Wurtz, K.-P. Ziock, L. Fabris, R. Graham, Comparing imaging and non-imaging techniques for reducing background clutter and resolving distant point sources 1 (2005) 338–342.
- [2] K. Vetter, L. Mihailescu, K. Nelson, J. Valentine, D. Wright, Gamma-ray imaging methods, Tech. rep., Lawrence Livermore National Laboratory (LLNL), Livermore, CA (2006).
- [3] B. R. Kowash, D. K. Wehe, N. O. Boyce, Extended source imaging using a single rotating modulation collimator, in: 2009 IEEE Nuclear Science Symposium Conference Record (NSS/MIC), 2009, pp. 1897–1901. doi:10.1109/NSSMIC.2009.5402165.
- [4] K. P. Ziock, J. W. Collins, L. Fabris, S. Gallagher, B. K. P. Horn, R. C. Lanza, N. W. Madden, Source-search sensitivity of a large-area, coded-aperture, gamma-ray imager, IEEE Transactions on Nuclear Science 53 (3) (2006) 1614–1621. doi:10.1109/TNS.2006.875285.
- [5] A. L. Hutcheson, B. F. Philips, E. A. Wulf, L. J. Mitchell, W. N. Johnson, B. E. Leas, Maritime detection of radiological/nuclear threats with hybrid imaging system., Homeland Security Affairs (2014) 1 – 5.
- [6] C. G. Wahl, Z. He, Gamma-ray point-source detection in unknown background using 3d-position-sensitive semiconductor detectors, IEEE Transactions on Nuclear Science 58 (3) (2011) 605–613. doi:10.1109/TNS.2011.2113355.

- [7] G. W. Phillips, Gamma-ray imaging with compton cameras, Nuclear Instruments and Methods in Physics Research Section B: Beam Interactions with Materials and Atoms 99 (1) (1995) 674 – 677, application of Accelerators in Research and Industry '94. doi:[https://doi.org/10.1016/0168-583X\(95\)80085-9](https://doi.org/10.1016/0168-583X(95)80085-9).
- [8] J. G. M. FitzGerald, A rotating scatter mask for inexpensive gamma-ray imaging in orphan source search: Simulation results, IEEE Transactions on Nuclear Science 62 (1) (2015) 340–348. doi:[10.1109/TNS.2014.2379332](https://doi.org/10.1109/TNS.2014.2379332).
- [9] J. Logan, D. Holland, L. Burggraf, J. Clinton, B. ODay, Monte carlo analysis of a novel directional rotating scatter mask photon detection system, IEEE Transactions on Nuclear Science 0 (submitted).
- [10] S. Agostinelli, J. Allison, K. Amako, J. Apostolakis, et al., Geant4a simulation toolkit, Nuclear Instruments and Methods in Physics Research Section A: Accelerators, Spectrometers, Detectors and Associated Equipment 506 (3) (2003) 250 – 303. doi:[https://doi.org/10.1016/S0168-9002\(03\)01368-8](https://doi.org/10.1016/S0168-9002(03)01368-8).
- [11] D. E. Holland, J. E. Bevins, L. W. Burggraf, B. E. ODay, Rotating scatter mask optimization for gamma source direction identification, Nuclear Instruments and Methods in Physics Research Section A: Accelerators, Spectrometers, Detectors and Associated Equipment 901 (2018) 104 – 111. doi:<https://doi.org/10.1016/j.nima.2018.05.037>.
- [12] R. J. Allemang, The modal assurance criterion twenty years of use and abuse, Sound and Vibration (2003) 14–21.
- [13] E. W. Weisstein, Hadamard matrix, From MathWorld—A Wolfram Web Resource. <http://mathworld.wolfram.com/HadamardMatrix.html>. Accessed 2017-17-08.
- [14] J. T. Goorley, M. R. James, T. E. Booth, F. B. Brown, J. S. Bull, L. J. Cox, J. W. Durkee Jr, J. S. Elson, M. L. Fensin, R. A. Forster III, et al., Initial mcnp6 release overview-mcnp6 version 1.0, Tech. rep., Los Alamos National Laboratory (LANL) (2013).